

Adaptive light-sheet microscopy for long-term, high-resolution imaging in living organisms

Loïc A Royer^{1,2}, William C Lemon¹, Raghav K Chhetri¹, Yinan Wan¹, Michael Coleman³, Eugene W Myers² & Philipp J Keller¹

Optimal image quality in light-sheet microscopy requires a perfect overlap between the illuminating light sheet and the focal plane of the detection objective. However, mismatches between the light-sheet and detection planes are common owing to the spatiotemporally varying optical properties of living specimens. Here we present the AutoPilot framework, an automated method for spatiotemporally adaptive imaging that integrates (i) a multi-view light-sheet microscope capable of digitally translating and rotating light-sheet and detection planes in three dimensions and (ii) a computational method that continuously optimizes spatial resolution across the specimen volume in real time. We demonstrate long-term adaptive imaging of entire developing zebrafish (*Danio rerio*) and *Drosophila melanogaster* embryos and perform adaptive whole-brain functional imaging in larval zebrafish. Our method improves spatial resolution and signal strength two to five-fold, recovers cellular and sub-cellular structures in many regions that are not resolved by non-adaptive imaging, adapts to spatiotemporal dynamics of genetically encoded fluorescent markers and robustly optimizes imaging performance during large-scale morphogenetic changes in living organisms.

Light-sheet fluorescence microscopy presents a powerful approach to live imaging of biological specimens^{1–7}, offering excellent spatial^{8–10} and temporal^{11–15} resolution and facilitating long-term observation of biological processes under physiological conditions^{16,17}. However, although it is feasible to achieve high spatial resolution close to the diffraction limit in small, transparent specimens, such as individual cells in culture or at the surface of multi-cellular organisms, it is generally difficult to achieve high-resolution images of larger, more optically challenging specimens such as entire embryos. These challenges are directly linked to the fundamental principle and key requirement in light-sheet microscopy: the laser light-sheet illuminating the specimen and the focal plane of the orthogonally oriented detection objective must be co-planar. Whenever and wherever this spatial relationship is violated, spatial resolution and image quality are degraded.

In practice, four main factors contribute to spatiotemporally varying mismatches between light-sheet and detection focal planes in live specimens. First, multicellular organisms typically have complex three-dimensional (3D) shapes. As the average refractive indices of the specimen, the surrounding support matrix (for example, agarose) and the medium in the microscope chamber (for example, water) usually differ substantially, light refraction occurs at the surface of the specimen and leads to mismatches in relative position and 3D orientation of light-sheet and detection planes. These mismatches change as the light sheet is moved to different regions of the specimen over the course of volumetric imaging. Second, the specimen itself has spatially varying optical properties as a result of local differences in cell density, cell size and biochemical composition (such as lipid-rich

yolk compared to tissue regions in *Drosophila* and zebrafish embryos). This spatial heterogeneity, which changes continuously during development, further impacts the direction and length of optical paths inside the specimen (Fig. 1a). Third, wavelength-dependent effects and chromatic aberrations introduce additional mismatches in light-sheet and detection planes that vary as a function of imaging depth and depend on the spectral illumination and detection windows of fluorescent markers. Fourth, fluorescent marker distributions frequently undergo spatiotemporal changes during imaging experiments, particularly in experiments involving the use of genetically encoded markers targeted to specific (potentially non-stationary) cell populations or the tracking of specific gene products (Fig. 1a). The spatial relationship of light-sheet and detection planes is thus subject to dynamic changes during the experiment that cannot be quantitatively accounted for at the beginning of the experiment.

Manually adapting the light-sheet microscope to the spatially variant optical properties of a specimen would be time consuming and involves a large number of parameters. It also cannot be done in advance, as the optical properties of the specimen will change during live imaging. Even at the beginning of an experiment, manual approaches are often not a realistic option considering that there is often only limited time available before the onset of the biological process of interest (for example, when imaging early developmental events^{18–20}) or the onset of specimen degradation (for example, when imaging sensitive organ explants¹⁵). Continuous manual monitoring and adaptation of the microscope to spatiotemporal changes in the living specimen during time-lapse imaging is practically not feasible. Systematically optimizing spatial resolution in large

¹Howard Hughes Medical Institute, Janelia Research Campus, Ashburn, Virginia, USA. ²Max Planck Institute of Molecular Cell Biology and Genetics, Dresden, Germany. ³Coleman Technologies Incorporated, Newtown Square, Pennsylvania, USA. Correspondence should be addressed to L.A.R. (royer@mpi-cbg.de) or P.J.K. (kellerp@janelia.hhmi.org).

Received 25 March; accepted 16 September; published online 31 October 2016; doi:10.1038/nbt.3708

living specimens thus requires a light-sheet microscope capable of automated spatiotemporally adaptive imaging.

Powerful approaches to adaptive optics are rapidly advancing deep-tissue imaging capabilities of point-scanning microscopy^{21,22}. In light-sheet microscopy, extended depth-of-field approaches^{23,24} could theoretically help reduce the impact of mismatches between light-sheet and detection focal planes, but the elongated detection point-spread function and poor light efficiency intrinsic to these methods dramatically reduces axial resolution and renders them unsuited to high-resolution live imaging. As an alternative, light-sheet-based adaptive optics approaches are under investigation, focusing on microscope system correction using fiducials²⁵ and snapshot imaging of tissue explants²⁶ and chemically fixed samples^{27,28}. However, until now, it has not been possible to realize spatiotemporally adaptive light-sheet imaging of living specimens.

Developing a method that addresses the key challenges outlined above is difficult for several reasons. At its core, a microscope design is needed with fully digitally adjustable opto-mechanical degrees of freedom for computer-controlled translation and rotation of light-sheet and detection focal planes in all dimensions. This microscope would have to be operated by an automated control framework that robustly assesses and systematically tracks spatial resolution and image quality across the specimen in real time. These spatiotemporal measurements must be designed to minimize impact on the specimen's photon budget, specimen physiology and microscope speed. The microscope's control software must furthermore be integrated with an optimization procedure capable of rapidly detecting if (and which) changes to the microscope's configuration are needed to recover and maintain maximum image quality across the specimen. The implementation of such a 'smart' light-sheet microscope, i.e., a combined hardware and software framework for automated spatiotemporally adaptive imaging, should furthermore be robust with respect to different biological model systems, biological processes, marker strategies, spatiotemporal signal dynamics and optical configurations of the microscope.

Here, we present such an integrated approach for spatiotemporally adaptive imaging. We demonstrate the capabilities and robustness of our method using a wide spectrum of (i) marker strategies, including different types of morphological markers and calcium indicators, (ii) model systems, including *Drosophila* and zebrafish embryos and zebrafish larval brains and (iii) imaging assays, including developmental, functional, multi-color and multi-view imaging experiments. We show that our method improves spatial resolution and signal strength two- to five-fold across large, multi-cellular organisms and recovers cellular and sub-cellular features in many regions that cannot be resolved by non-adaptive light-sheet microscopy.

RESULTS

Spatiotemporally adaptive light-sheet microscopy

We developed an automated multi-view light-sheet microscope that systematically assesses and optimizes spatial resolution across living organisms by adapting to the optical properties of the specimen and its environment. The control software of this microscope, which we termed the AutoPilot framework, continuously adapts to dynamic changes in the specimen in order to maintain optimal image quality over the course of long-term, high-speed imaging experiments. All decisions are data driven and based on real-time evaluation of image-derived information collected using time- and light-efficient procedures operating in the background of the experiment.

The core of our method for spatiotemporally adaptive imaging consists of five integrated components: (i) a multi-view light-sheet

microscope with ten digitally adjustable mechano-optical degrees of freedom for translating and rotating light-sheet and detection focal planes in three dimensions, (ii) a real-time control software that operates these degrees of freedom and facilitates spatiotemporal microscope adaptation during high-speed, volumetric live-imaging experiments, (iii) a general algorithm for fast and robust assessment of local image quality, (iv) an automated method for image-based mapping of the 3D light-sheet geometry inside a fluorescently labeled specimen, and (v) a general algorithm for data-driven optimization of the configuration of light-sheet microscopes capable of multi-color imaging with multiple illumination and detection arms. Below, we will summarize the architecture and capabilities of this framework. Details are provided in the **Supplementary Methods**.

To achieve fast and accurate digital adjustability of all degrees of freedom essential for adaptive imaging (**Fig. 1b**), our multi-view microscope (component (i), **Supplementary Methods**, part 1; **Supplementary Fig. 1**) provides two sets of galvanometer scanners in each illumination arm for light-sheet rotation in sample space (parameters α_1 , α_2 , β_1 and β_2 ; **Supplementary Fig. 2**) and light-sheet translation perpendicular to the illumination axis (parameters I_1 and I_2). Light-sheet waists and detection focal planes can be translated along their optical axes using illumination and detection objectives mounted on piezo positioners (parameters Y_1 , Y_2 , D_1 and D_2). The scanners and piezos are operated and synchronized by a real-time controller (component (ii)) capable of precise, nonlinear adjustment of all parameters during high-speed volumetric imaging.

Fully automated spatiotemporally adaptive imaging critically requires a fast and robust algorithm for estimating and quantitatively comparing image quality in different system states (component (iii)). This in turn demands a reliable image quality metric that is highly sensitive to changes in resolution. We systematically compared and improved upon the best image quality metrics available in the literature by evaluating 30 conventional and modified candidate metrics on 66 image data sets covering a wide spectrum of biological model systems, marker strategies and imaging assays (**Supplementary Methods**, part 2; **Supplementary Fig. 3**). Using synthetic- (**Supplementary Tables 1 and 2**) and real-data (**Supplementary Tables 3 and 4**) benchmarks, we identified the Shannon entropy of the normalized discrete cosine transform (DCTS) as the optimal metric for light-sheet fluorescence microscopy. The DCTS offers the best focus localization accuracy (mean error of 330 nm for a light sheet full-width at a half-maximum thickness of 3.0 μm and a detection depth of focus of 1.75 μm), high signal-to-background ratio near the global optimum and low density of local maxima along the focus curve, while operating at a median processing speed of 27 ns per pixel (**Supplementary Tables 1–4**; **Supplementary Figs. 4–7**).

To minimize the impact of AutoPilot measurements on the acquisition speed, the AutoPilot framework monitors image quality exclusively during the idle time between time-point acquisitions (using less than 5% of the total microscope bandwidth) and quickly searches for better parameter settings at user-defined 'reference planes' distributed throughout the specimen volume (typically 4–8 planes that partition the volume in 20–80 μm steps) (**Supplementary Fig. 8**). To minimize AutoPilot measurements in these reference locations, we developed an algorithm capable of computing optimal settings for three parameter classes simultaneously from a single defocus image sequence. This algorithm (component (iv)) reconstructs the 3D light-sheet geometry inside the sample and thereby determines light-sheet angles α_i and β_i as well as light-sheet defocus offsets I_i (**Supplementary Methods**, part 5). To optimize robustness across a wide range of marker strategies, including uniform textureless marker distributions, light-sheet

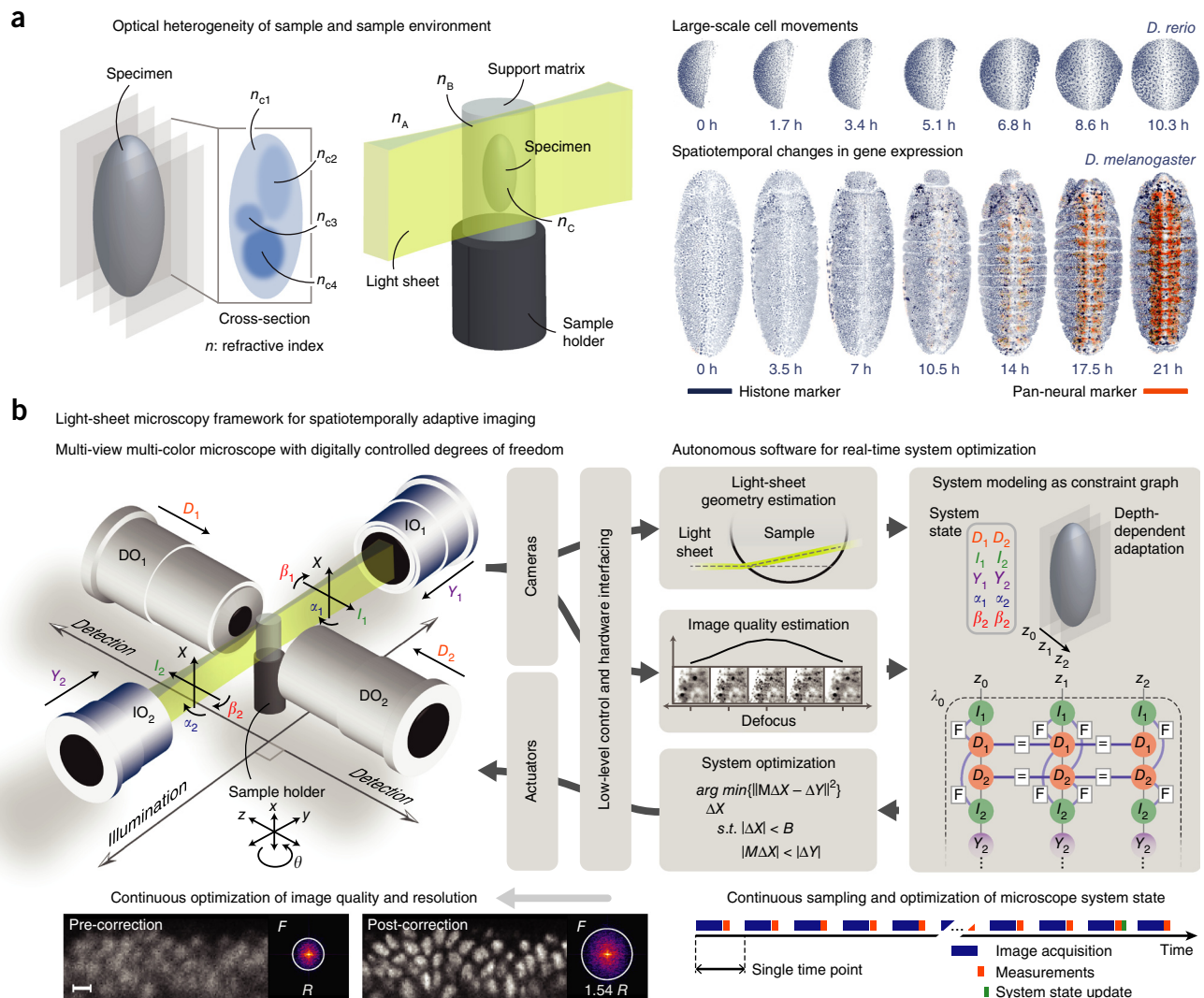


Figure 1 Spatiotemporally adaptive light-sheet microscopy. **(a)** Fundamental optical challenges associated with long-term live imaging of large biological specimens often lead to loss of spatial overlap between illuminating light sheets and detection focal planes in light sheet microscopy. The most severe problems are caused by spatial and temporal heterogeneity of the refractive index across the live specimen, the surrounding support matrix and the medium in the sample chamber (left). Thermal, mechanical and electronic drifts in microscope components during live imaging can further contribute to a degradation of spatial resolution (**Supplementary Video 10**). When imaging developing organisms, such as early zebrafish (*D. rerio*) embryos during epiboly (top right), one also needs to consider that optical conditions change continuously as a function of time and spatial location in the sample. Live imaging of genetically encoded fluorescent markers, such as a pan-neural fluorescent marker tracking the developing nervous system in *Drosophila* (bottom right), is further complicated by spatiotemporal dynamics in marker expression. Recovering optimal resolution in the imaging experiment thus requires spatiotemporal adaptation of the microscope to the dynamic optical conditions while tracking dynamic fluorescent signals. **(b)** Overview of the fully automated light-sheet microscopy framework for spatiotemporally adaptive imaging, which addresses the challenges outlined in **a**. Our framework consists of (i) a multi-view light-sheet microscope with ten digitally adjustable degrees of freedom that control 3D offsets and 3D angles between light sheets and detection focal planes, and (ii) a real-time software layer that autonomously monitors image quality throughout the imaging volume and automatically and continuously adjusts these degrees of freedom to optimize spatial resolution and image quality across the sample in space and time. Scale bar, 5 μm .

geometry and defocus are optionally mapped with a structured light sheet created by high-frequency laser intensity modulation. In this mode, an engineered high-frequency component¹⁹ is introduced to the images to ensure robustness of auto-focusing independently of the (*a priori* unknown) native frequency content of the image data, whereas primary data acquisition is performed with a conventional, uniform light sheet. In addition to enhancing robustness, the use of structured light sheets for focus localization further reduces the energy load on the sample.

The AutoPilot measurements performed across the specimen volume for all ten degrees of freedom are collectively used to formulate an

optimization problem, from which a new, optimal state of the microscope is computed (**Supplementary Methods**, parts 3 and 4). This optimization procedure (component (v)) employs a constraint graph, a mathematical object that represents the opto-mechanical degrees of freedom of the microscope and their spatial, temporal and spectral relationships (**Supplementary Fig. 9**). In the constraint graph, nodes represent the degrees of freedom and edges define constraints that are either fixed or dynamic in nature (**Supplementary Fig. 9a**). Fixed constraints encode invariant geometrical and optical requirements, for example, enforcing continuity in image space across the two camera fields and aligning image data in multiple color channels.

Dynamic constraints relate to image quality measurements, presence or absence of local signal and local light-sheet geometry in the sample. In case of temporally dynamic or spatially sparse fluorescence-marker distributions, substitution constraints automatically tackle the lack of fluorescence signal at certain time points and at certain spatial locations in the specimen (**Supplementary Fig. 9d**).

Rapid recovery of optimal resolution after perturbations

To evaluate the performance of our framework, we performed a system benchmark using well-defined optical perturbations of known magnitude. This benchmark served as a validation and characterization of our method before subjecting the framework to the *a priori* unknown optical perturbations encountered in the biological experiments described in the next sections.

We performed a short-term volumetric imaging experiment using a live *Drosophila* embryo while electronically inducing well-defined, instantaneous jumps and continuous drifts of light-sheet and detection focal plane positions of varying magnitudes (jumps of 2–8 μm , drifts of 1 $\mu\text{m min}^{-1}$). These perturbations were generated using the piezo controllers responsible for positioning light sheets and detection objectives (**Supplementary Fig. 1**), ensuring that the microscope control framework itself was unaware of the timing, type and source of these external events. The AutoPilot framework could thus assess and compensate for these perturbations only through real-time analysis of the acquired images, mimicking the challenges encountered in an actual biological imaging experiment. By comparing the magnitude and type of induced system perturbations to decisions and response timing of the AutoPilot framework, we quantitatively assessed AutoPilot performance (**Supplementary Video 1; Supplementary Fig. 10; Supplementary Table 5**). This benchmark demonstrates the rapid and accurate recovery of optimal image quality in response to a variety of perturbations affecting the 3D spatial relationship between light sheets and focal planes; for all perturbations, the AutoPilot framework correctly identified the affected degree(s) of freedom affected and recovered, on average, 92% of the perturbation-induced loss in image quality within 1–2 time points after a perturbation.

We performed additional benchmarks for the angular degrees of freedom by introducing and compensating for light-sheet deflections of known magnitude (jumps of 0.25–2°). These latter experiments show that the AutoPilot framework correctly identifies and corrects angular mismatches between light-sheet and detection focal planes

inside living specimens with a precision of 0.15° and 0.21° for α_i and β_i , respectively (**Supplementary Fig. 11**).

Finally, we assessed how quickly the AutoPilot framework optimizes an uncorrected microscope *de novo* (starting in an unknown state) and recovers high spatial resolution across a large specimen. We measured the system correction time for an entire zebrafish larval brain expressing a genetically encoded calcium indicator¹² (**Supplementary Fig. 12**). We subdivided the 800 × 600 × 200 μm^3 specimen volume into five reference regions and executed three rounds of iteratively converging parameter adaptation to the optical properties of the specimen (**Supplementary Fig. 12a**), confirming that optimal system performance was reached in the last round (**Supplementary Fig. 12b**). After starting with a complete lack of cellular resolution throughout the brain, system optimization took 40 s and systematically recovered high resolution throughout the brain (**Supplementary Fig. 12c**). We note that this whole-system optimization procedure (“Initial system optimization”, Online Methods) is only required once, at the beginning of a time-lapse experiment, to ensure that the microscope is in a well-defined, optimal state. Subsequent system state updates do not require iterative schemes and can be partitioned into subsets of measurements to minimize time spent on AutoPilot tasks (“Microscope state updates”; ≤ 3 s of continuous AutoPilot activity corresponding to $\leq 5\%$ of microscope bandwidth; **Fig. 1b**).

Spatiotemporally adaptive imaging of *Drosophila* development

A fundamental challenge for high-resolution live imaging of multicellular organisms is the occurrence of dynamic changes of local optical properties, in particular, during changes in specimen morphology. We thus evaluated the potential of spatiotemporally adaptive imaging in this scenario using *Drosophila* embryonic development as a challenging test case.

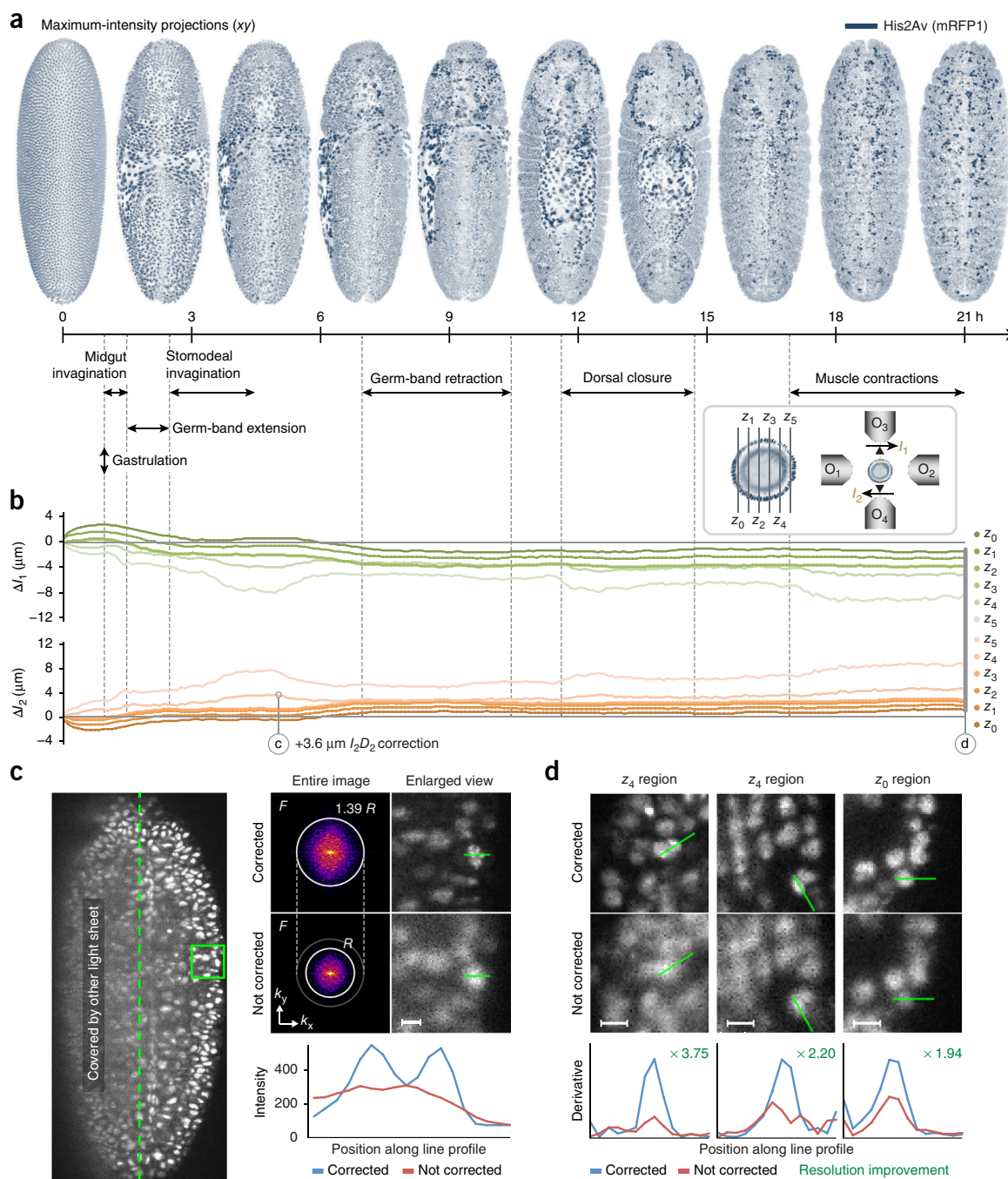
In early stages of embryogenesis, morphological changes occur across the entire embryo and manifest themselves in fast rearrangements and remodeling of tissues. Moreover, the early *Drosophila* embryo contains a large amount of lipid-rich yolk that is consumed over time. These processes affect local optical properties throughout the specimen and degrade spatial resolution and image quality if left unaccounted for.

We conducted a 21-h time-lapse imaging experiment with a *Drosophila* embryo expressing histone–red fluorescent protein (histone–RFP) in all cells (**Supplementary Videos 2–4**). The AutoPilot framework had full control of this experiment and was allowed to

Figure 2 Spatiotemporally adaptive imaging of *Drosophila* embryonic development. **(a)** Dorsoventral maximum-intensity projections of a *D. melanogaster* embryo expressing RFP in all cell nuclei (w;His2Av-mRFP1;+), representing a 21-h time-lapse experiment using spatiotemporally adaptive imaging (**Supplementary Video 2**). Landmark developmental processes are annotated on the experiment time axis. Imaging started in the blastoderm stage (“0 h” on the time axis), corresponding to 3 h after egg laying (h AEL). The embryo is ~500 μm long and ~200 μm wide. **(b)** Plots visualizing real-time corrections of the positions of light sheets 1 (green) and 2 (orange) relative to the respective detection focal planes as a function of time and spatial location in the embryo. These corrections were computed by the real-time software layer of the adaptive imaging framework to maximize spatial resolution throughout the specimen. Using a fully automated workflow, image quality in the embryo was sampled, evaluated and optimized at six reference planes (z_0 – z_5 , top right inset). **(c)** Improvements in spatial resolution and image quality achieved by spatiotemporally adaptive imaging. Example image data are shown for the spatial location marked in **b** at 5 h. Fourier analysis of the microscopy data acquired with (top) and without (bottom) microscope state corrections computed by the adaptive imaging framework demonstrates a 39% increase in the cut-off radius in frequency space across the entire image plane. Enlarged views (right) and line profiles (below) show that spatiotemporally adaptive imaging recovered cellular and sub-cellular features that were not resolved with non-adaptive imaging. Images labeled “not corrected” were acquired using the optimized microscope parameter settings determined by the AutoPilot framework at the beginning of the experiment (“Initial System optimization”, Online Methods). Thus the difference between “corrected” and “not corrected” settings shown here and in **d** is a lack of continuous microscope adaptation over the course of the experiment for images labeled as “not corrected.” A comprehensive side-by-side comparison is shown as a function of space and time in **Supplementary Videos 3 and 4**. **(d)** Side-by-side comparison of image quality and spatial resolution in representative image regions for adaptively corrected (top row) and uncorrected (middle row) microscope states at 21 h. Increase in spatial resolution (factors in green) was quantified by comparative analysis of the derivatives of intensity line profiles crossing sharp edges in the image data, corresponding to boundaries of fluorescently labeled cell nuclei (bottom row). The computational procedure and its mathematical derivation are described in **Supplementary Methods**, part 6. The complete set of *Drosophila* example image data is presented in **Supplementary Figure 14**. Scale bars, 20 μm (c, left), 5 μm (c, right; d).

adjust the main degrees of freedom (I_1 , I_2 , D_1 and D_2) to continuously and automatically optimize the microscope system state (Fig. 2; Supplementary Fig. 13; Supplementary Table 6). These four degrees of freedom required for translating light-sheet and detection focal planes form the minimal parameter set needed for effective system corrections. Advanced adaptive imaging with all ten degrees of freedom will be discussed in the next results sections. As expected, the corrections required for optimal spatial resolution (Fig. 2b) vary as a function of time and depend on the imaging depth inside the embryo. Across space and time, light-sheet positions needed to be adjusted by 5.3 μm on average (up to 9.4 μm , at maximum) across all reference locations (Fig. 2b). The real-time corrections performed by the AutoPilot framework furthermore demonstrate that the most

pressing need for system-state adjustments arises between 3 and 8 h after egg laying (corresponding to 0–5 h in Fig. 2a,b), when the fastest and most-pronounced internal morphological changes in the embryo take place. Spatial resolution is substantially improved throughout the imaging experiment, and cellular and sub-cellular features are recovered in many regions that would suffer from low image quality in non-adaptive microscopy (Fig. 2c; Supplementary Video 3) including in deep-tissue regions of the developing nervous system (Supplementary Video 4). We quantified improvements in spatial resolution throughout the embryo by systematically analyzing intensity profiles crossing cell nuclei boundaries (Fig. 2d; Supplementary Fig. 14; Supplementary Methods, part 6). This analysis shows that adaptive imaging improved spatial resolution by an average of 2.4-fold



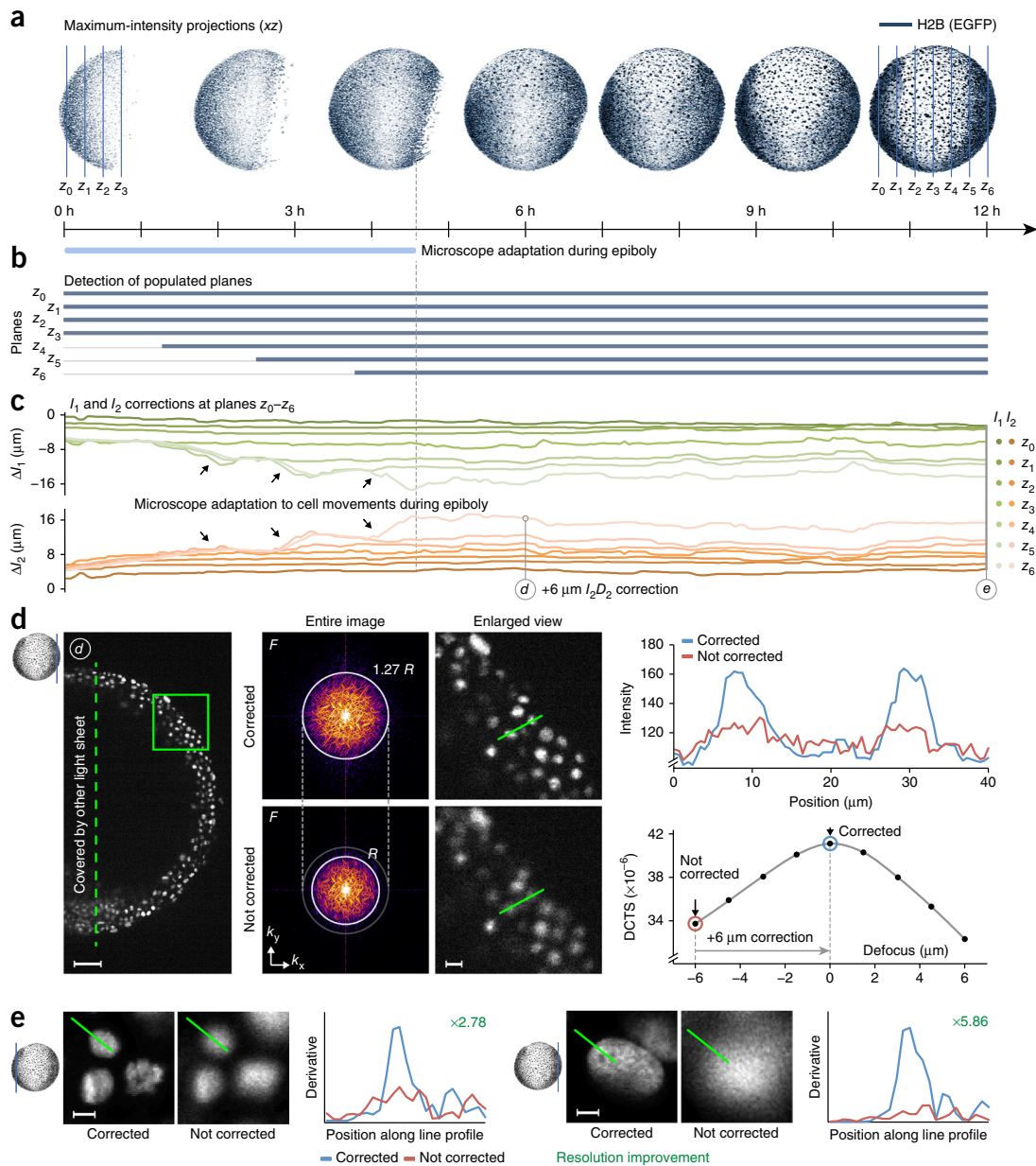


Figure 3 Spatiotemporally adaptive imaging of zebrafish embryonic development. **(a)** Lateral maximum-intensity projections of a *D. rerio* embryo expressing GFP in all cell nuclei (H2B–eGFP), representing a 12-h time-lapse experiment using spatiotemporally adaptive imaging with degrees of freedom D_i and I_i ($i = 1, 2$; **Supplementary Video 5**). Imaging started in the 30%-epiboly stage (“0 h” on the time axis), corresponding to 5 h post fertilization. The embryo is $\sim 700 \mu\text{m}$ in diameter. **(b)** As fast, coordinated cell movements spread the blastoderm across the large, central yolk cell (see **a**), the adaptive light-sheet-based imaging framework continuously adjusts the microscope system state to maintain optimal image quality. To facilitate this spatiotemporal adaption in imaging experiments with dynamic fluorescence signals, the framework automatically flags reference locations lacking fluorescence signal (thin gray lines) and monitors the emergence of fluorescence signal as a function of time and spatial location in the specimen (thick blue lines). Note the continuous spreading of the blastoderm across the yolk cell and the concomitant detection of fluorescence signal in corresponding reference locations z_4 – z_6 during the first 4 h of the experiment. **(c)** Plots visualizing real-time corrections of the positions of the two light sheets (green and orange) relative to the respective detection focal planes as a function of time and spatial location in the embryo (reference planes z_0 – z_6 ; see **a**). Corrections in regions lacking fluorescent signals are guided by neighboring reference planes until local fluorescent signal emerges and is used to determine region-specific microscope state corrections. **(d)** Improvements in spatial resolution and image quality achieved by spatiotemporally adaptive imaging. Example image data are shown for the spatial location marked in **c** at 6 h. Fourier analysis of data (second column) acquired with (top) and without (bottom) microscope corrections computed by the adaptive imaging framework demonstrates a 27% increase in cut-off radius in frequency space. Enlarged views and line profiles (right) show that adaptive imaging recovered cellular and sub-cellular features that were not resolved by non-adaptive imaging. Defocus aberrations up to 6 μm occur without adaptive imaging (bottom right, DCTS values for AutoPilot image defocus series). **(e)** Side-by-side comparison of image quality and spatial resolution in two representative image regions for adaptively corrected (degrees of freedom D_i , I_i , Y_i , α_i and β_i with $i = 1, 2$) and uncorrected microscope states at the end of epiboly. Locations of image planes are indicated in illustrations to the left of each image panel. Increase in spatial resolution (factors in green) was quantified using derivatives of line profiles crossing sharp edges in the images corresponding to boundaries of fluorescently labeled cell nuclei. See **Supplementary Videos 6** and **7** for a systematic side-by-side comparison of images in corrected and uncorrected microscope states. The procedure and its mathematical derivation are described in **Supplementary Methods**, part 6. The complete set of zebrafish example image data is presented in **Supplementary Figure 15**. Scale bars, 50 μm (**d**, left), 10 μm (**d**, right), 5 μm (**e**).

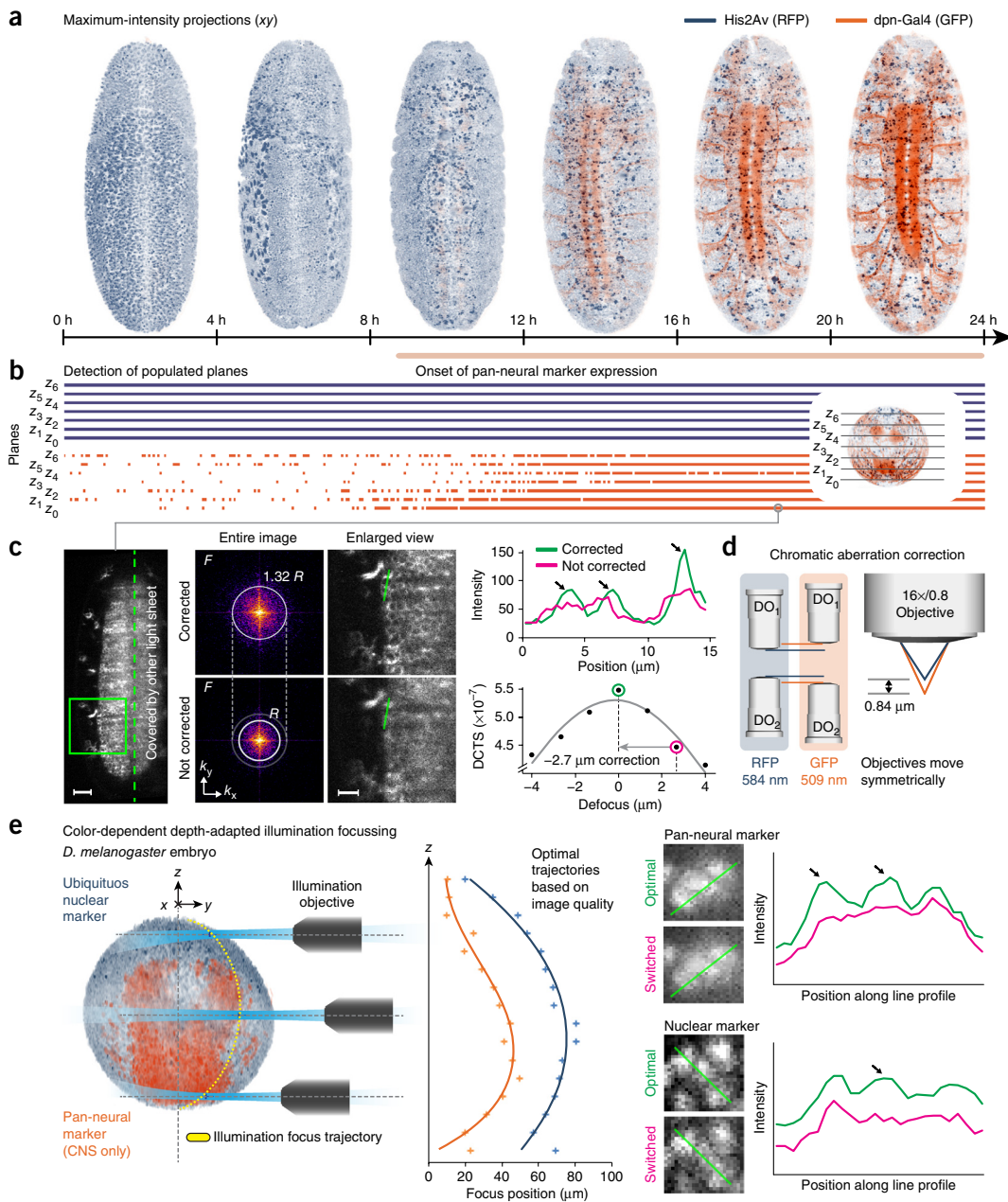


Figure 4 Spatiotemporally adaptive imaging of dynamic gene expression patterns. **(a)** Dorsoventral maximum-intensity projections of a *D. melanogaster* embryo expressing RFP in all cell nuclei and GFP in the nervous system (deadpan^{EE}-Gal4, UAS-myrr::GFP, His2Av-RFP), representing a 20-h time-lapse experiment using spatiotemporally adaptive imaging (**Supplementary Video 8**). Imaging started in the blastoderm stage (“0 h” on the time axis), corresponding to 3 h AEL. Expression of the pan-neural marker starts at around 10 h. **(b)** The onset of expression of the pan-neural marker is automatically detected by the adaptive imaging framework, which optimizes all parameters associated with this color channel in response to the emerging signal. Note that the onset of expression occurs slightly earlier in ventral regions (reference planes Z_0 , Z_1 , and Z_2). **(c)** Improvements in spatial resolution and image quality achieved by spatiotemporally adaptive imaging. Example image data are shown for the spatial location marked in **b** at 18.5 h. Fourier analysis of the microscopy data (second column) acquired with (top) and without (bottom) microscope state corrections computed by the adaptive imaging framework demonstrates a 32% increase in cut-off radius in frequency space. Enlarged views and line profiles to the right show that adaptive imaging recovered cellular and sub-cellular features that were not resolved with non-adaptive imaging. Plot to the bottom right shows DCTS values determined by AutoPilot for a defocus series acquired at the image location shown to the left, indicating optimal image quality in the corrected system state. **(d)** The adaptive imaging framework automatically corrects for focal shifts between different color channels arising from chromatic aberrations inherent to the design of the detection objectives. For the Nikon 16 \times /0.8 objectives used in this experiment, the framework compensated for a focal shift of 0.84 μm between GFP and RFP detection bands. **(e)** The adaptive imaging framework automatically optimizes the position of the beam waist of the illuminating Gaussian laser beams (position of minimal light-sheet thickness) by real-time adjustment of the positions Y_1 and Y_2 of the illumination objectives during volumetric imaging (left). In multi-color imaging experiments, the illumination focus trajectory is analyzed for each color channel separately and optimally adapted to the respective spatial distribution of each fluorescent marker (middle: blue, ubiquitous nuclear RFP; orange, pan-neural GFP). To maximize resolution, different illumination focus trajectories are needed for the ubiquitous and pan-neural markers used in this experiment: switching illumination focus trajectories assigned to the two-color channels degrades spatial resolution substantially, leading to a loss of cellular resolution (see images labeled “Switched” vs. “Optimal” and corresponding line profiles shown at right). Scale bars, 20 μm (c, left), 10 μm (c, right).

(up to 3.8-fold locally) and signal strength by an average of 1.6-fold (up to 2.0-fold locally). Fourier analysis of the data acquired by adaptive imaging indicates an increase of 30–40% in the radius, marking maximum frequency support (Fig. 2c). This analysis underestimates the improvement in resolution compared to the line profile analysis because the band-limited and noisy image is considered as a whole, including regions that only contain low-frequency structures irrelevant for estimating resolution limits (Supplementary Methods, part 6). Furthermore, in the interest of fair comparison, our quantifications generally underestimate AutoPilot performance: images representing the uncorrected microscope state were acquired using the fully optimized microscope configuration determined by the AutoPilot framework at the beginning of the time-lapse imaging experiment. Thus, this analysis solely quantifies improvements attributable to continuous microscope state updates during live imaging.

Adaptive imaging of large-scale cell movements in zebrafish

In the imaging experiment discussed above, the *Drosophila* embryo undergoes large-scale morphological changes during early development, but a fluorescent signal is available at all times throughout the ubiquitously labeled embryo. In experiments with other model systems, developmental processes or marker strategies, the distribution of fluorescent signal can change substantially as a function of time. Thus, we next set out to perform on-demand microscope adaptation to large-scale changes in signal distribution as a result of morphological changes. To this end, we performed spatiotemporally adaptive imaging of developing zebrafish embryos throughout gastrulation. Our 6- to 12-h-long experiments capture the entire process of epiboly (Supplementary Videos 5–7), which is characterized by large-scale directed cell movements across the embryo (Fig. 3a). Thus, the microscope must continuously monitor the specimen volume for the emergence of local signal and rapidly adapt, on demand, to new regions that previously lacked fluorescent signal (Fig. 3b).

During the first 4.5 h of the 12-h time-lapse experiment shown in Supplementary Video 5, cells expressing nuclear-localized GFP move from the animal to the vegetal hemisphere and progressively populate the initially empty reference planes z_4 – z_6 (Fig. 3a). The AutoPilot framework automatically detects the associated spatiotemporal changes in fluorescence and adapts the microscope to those newly populated regions (Fig. 3b,c; Supplementary Table 7). The density of reference planes is set sufficiently high to ensure adequate correction of spatially varying optical properties. A practical

choice is a setting at which differences in light-sheet offset corrections for neighboring planes do not exceed the depth of focus ($\sim 2 \mu\text{m}$, resulting in 7 reference planes across the zebrafish embryo; Fig. 3c). These settings are typically robust across all experiments performed with the same biological model system. If no previous AutoPilot measurements are available, a high density of reference planes (for example, 20- μm spacing) can be used to assess optical effects while ensuring optimal image quality already in the first experiment. Empty reference planes are subjected to the same parameter changes as their closest spatial neighbors for which fluorescence signal is available.

During large-scale cell movements, the microscope progressively adapts to changes in the imaging volume and locally optimizes image quality as soon as measurements based on local signal become available. As shown above for *Drosophila* development, spatiotemporally adaptive imaging also offers substantial improvements in spatial resolution and image quality for developing zebrafish embryos, recovering cellular and even sub-cellular features in many regions that are not resolved by non-adaptive imaging (Fig. 3d). Quantitative analysis of resolution shows that adaptive imaging improved spatial resolution an average of 3.1-fold (up to 5.9-fold locally) and signal strength an average of 2.1-fold (up to 4.8-fold locally) (Fig. 3e; Supplementary Fig. 15; Supplementary Methods, part 6). Fourier analysis of the data acquired by adaptive imaging furthermore indicates an increase of 20–30% in the radius marking maximum frequency support (Fig. 3e). A side-by-side comparison of image quality in non-adaptive and spatiotemporally adaptive imaging, using AutoPilot control of all degrees of freedom ($\alpha_1, \alpha_2, \beta_1, \beta_2, I_1, I_2, Y_1, Y_2, D_1$ and D_2 , Supplementary Table 8), is shown for different regions of the embryo in Supplementary Videos 6 and 7.

Adaptive multi-color imaging of dynamic gene expression

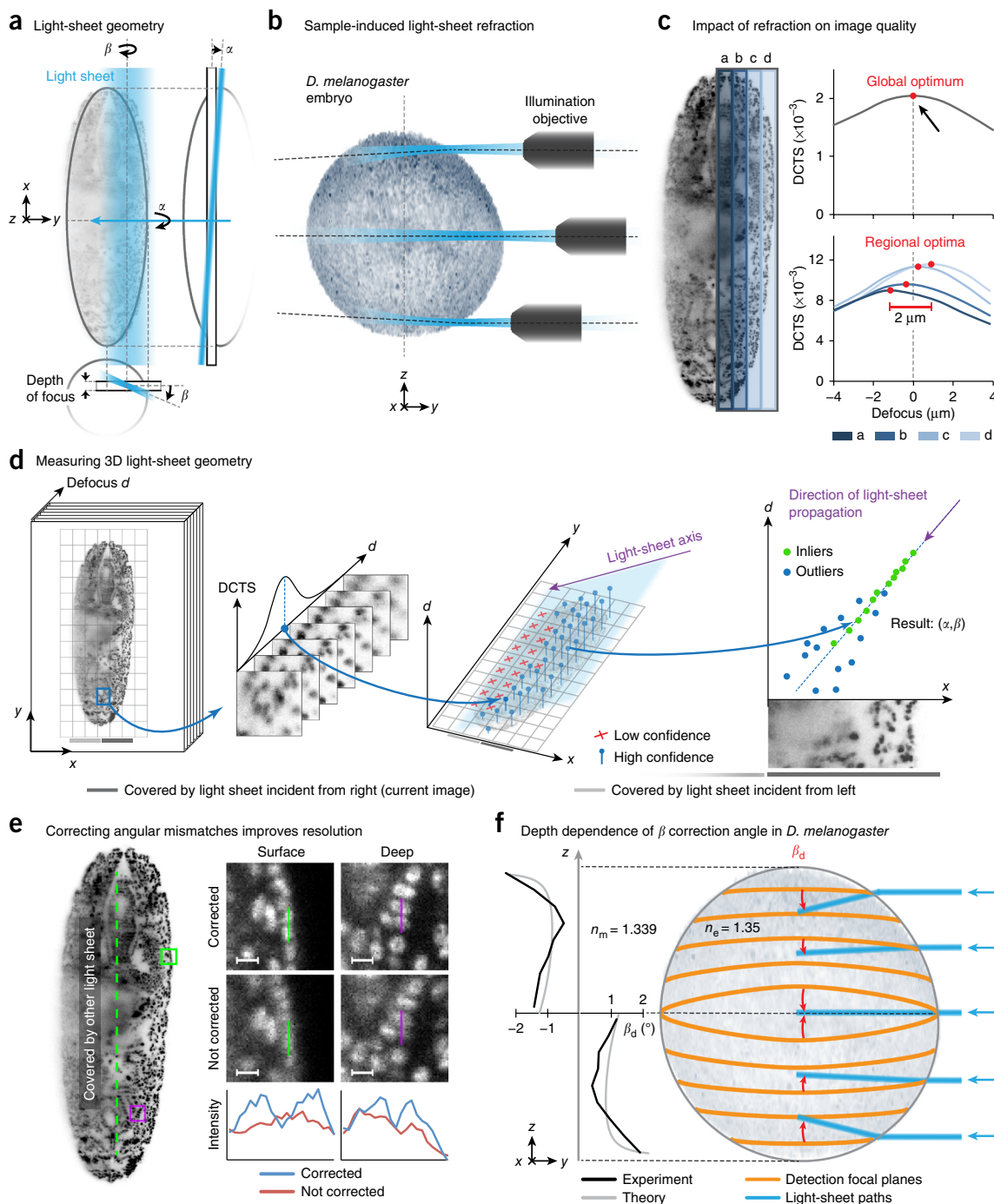
Multi-color imaging is a powerful tool for interrogating dynamic processes in living organisms. Key applications include, for example, the study of protein–protein interactions and the registration of cell-type-specific information to the local tissue context. The spatial distributions of the respective markers frequently undergo dynamic changes, and genetic labels tracking specific gene products may not even be expressed at the beginning of a time-lapse experiment. To demonstrate ‘on demand’ microscope adaptation to *a priori* unknown marker distributions in a multi-color setting, we followed cellular dynamics for 20 h in entire developing *Drosophila*

Figure 5 Spatiotemporally adaptive optimization of the 3D light-sheet path *in vivo*. (a) In addition to the positions of detection focal planes (D), lateral light-sheet offsets (l) and axial positions of light-sheet waists (Y), the adaptive imaging framework also optimizes the 3D orientation of light sheets by adjusting angular degrees of freedom α and β . (b) On first principles, the light-sheet angle β inside a live specimen is expected to change between image planes as a result of refraction at the interface between mounting matrix³⁶ ($n_m \approx 1.339$) and specimen³⁷ ($n_e \approx 1.35$ for cytosol). By contrast, the light-sheet angle α is not expected to vary across ovoid-shaped samples if their short axis is aligned with the illumination axis. (c) If light-sheet and detection focal planes are co-planar outside the sample but tilted with respect to each other inside the sample, not all sample regions illuminated by the light sheet are in focus simultaneously. At a depth of 50 μm in a *Drosophila* embryo, optimal focus settings change continuously across the image plane (see regions a, b, c and d), leading to a 2- μm focus spread that corresponds to $\beta = 0.6^\circ$. (d) The 3D orientation of the light sheet in the sample is automatically determined with a three-step algorithm: first, acquisition of a symmetric defocus stack; second, division of stack into sub-regions, DCTS focus curve computation for each sub-region, and determination of points (x, y, d) characterizing the 3D light-sheet path; third, detection of outliers and robust reconstruction of angles α and β between light-sheet and detection focal plane. (e) Measuring and correcting angular mismatches α and β between light sheets and detection focal planes improves spatial resolution beyond the level achieved by spatiotemporally adaptive imaging restricted to degrees of freedom D, l and Y . Representative examples of superficial and deep image regions in a *Drosophila* embryo are shown as enlarged views (purple, green) acquired with (top) and without (bottom) adaptive optimization of α and β . Line profiles (bottom) reveal sub-cellular features that are not resolved by correcting only D, l and Y . (f) Experimentally measured and theoretically predicted (black and gray lines in β -plot) correction angles β across the volume of a *D. melanogaster* embryo. Predictions were obtained with a ray optics model that assumes average refractive indices of 1.339 and 1.35 of matrix³⁶ and surface regions in the embryo³⁷, respectively. The good agreement between experiment and model suggests that two main optical effects are responsible for angular mismatches of light sheets and detection focal planes inside the sample: (i) light-sheet refraction at the interface between embryo and surrounding matrix/medium, and (ii) curvature of detection focal planes inside the sample as a result of sample-induced lensing along the optical detection path. Scale bars, 5 μm (e).

embryos expressing nuclear-localized RFP in all cells and cytoplasmic GFP in precursor cells forming the embryonic nervous system (Supplementary Video 8; Fig. 4a; Supplementary Table 9). Thus, in addition to adapting to optical changes in the developing embryo, the AutoPilot framework must autonomously detect the onset of GFP expression in different parts of the specimen and adapt to the continuously changing distribution of GFP throughout the embryo. The two-color channels furthermore need to be correctly registered in space, which requires automated detection and compensation of chromatic aberrations.

By tracking the spatiotemporal expression of the pan-neural marker (Fig. 4b), the AutoPilot framework evaluates which measurements

provide information for improving local image quality and substitutes data points corresponding to regions with low signal. This selective optimization procedure robustly improves spatial resolution throughout the embryo and resolves individual cells in many parts of the emerging nervous system that lack cellular resolution without adaptive imaging (Fig. 4c). Specimen- and optics-induced chromatic aberrations are automatically detected and eliminated (Fig. 4d). Moreover, by controlling the positions of the illumination objectives (Y_1 and Y_2), the AutoPilot framework ensures that the thinnest regions of the light sheets systematically track the 3D marker distribution across the specimen (Supplementary Fig. 16). Because the ubiquitous (RFP) and pan-neural (GFP) markers are distributed differently in space,



the AutoPilot framework further improves spatial resolution by determining optimal illumination focus trajectories for each color channel individually (Fig. 4e; Supplementary Fig. 16f,g).

Compensation of 3D light-sheet refraction in living embryos

In addition to adapting the positions of light-sheet planes, light-sheet waists and detection focal planes (Fig. 1b), the AutoPilot framework

controls the 3D angles between light-sheet and detection focal planes (α_1 , α_2 , β_1 and β_2 ; Fig. 5a). These degrees of freedom are essential to compensate for spatially variant light-sheet refraction at the interface between the specimen and its environment. Without spatial adaptation of light-sheet angles, the corresponding loss of co-planarity between light-sheet and detection focal planes degrades spatial resolution and image quality, as it becomes impossible to focus across the entire field

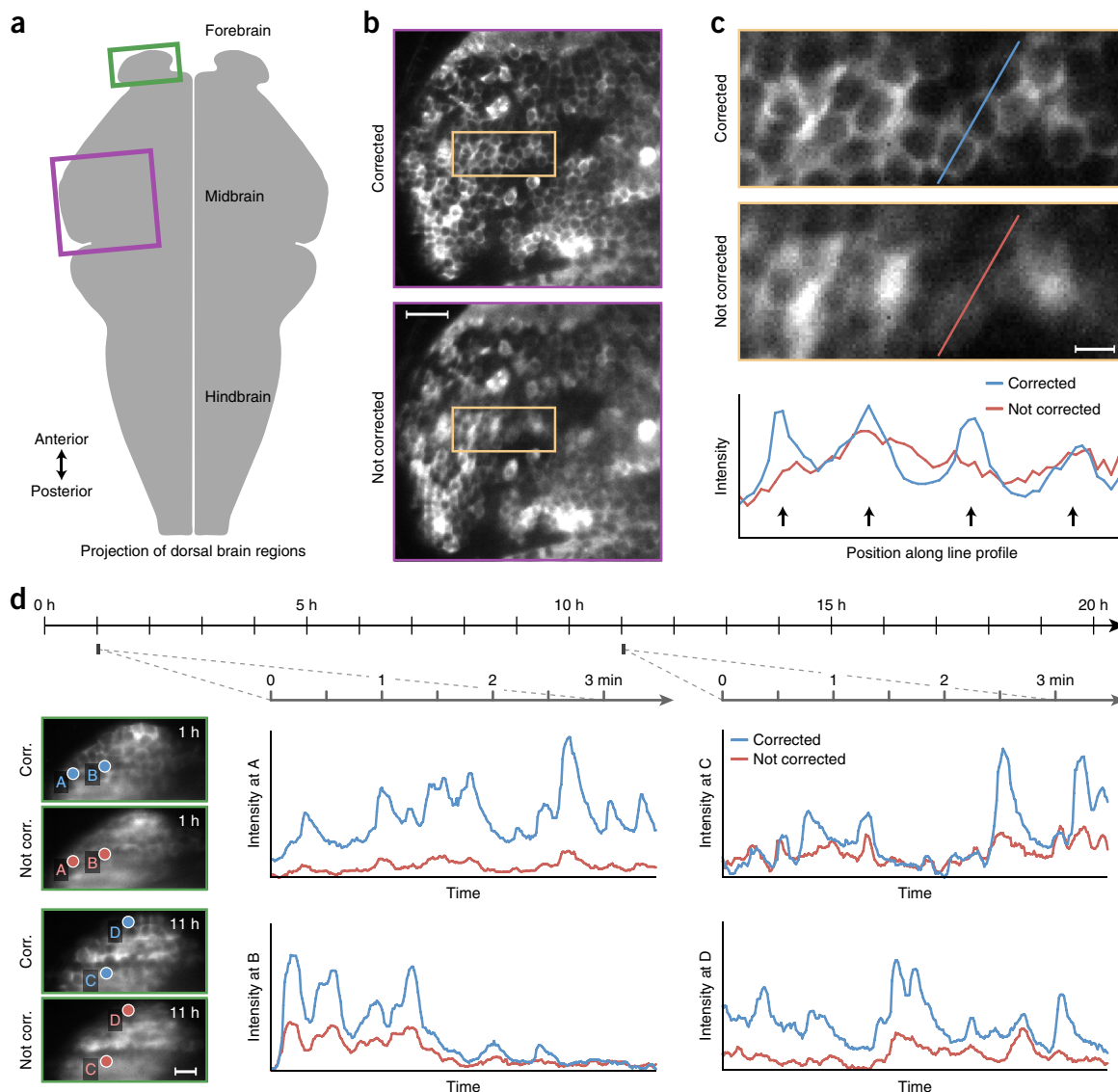


Figure 6 Spatiotemporally adaptive whole-brain functional imaging in larval zebrafish. (a) Geometrical outline of dorsal half of a zebrafish larval brain viewed from a dorsal perspective. Magenta and green boxes indicate the locations of the image data shown in b and d, respectively. (b) Side-by-side comparison of image quality and spatial resolution in adaptively corrected and uncorrected image data of a representative midbrain region after 11 h of whole-brain functional imaging in a 4-d-old *Tg(elavl3:GCaMP6f)* zebrafish larva (Supplementary Table 10). A detailed side-by-side comparison of multiple brain regions captured in this spatiotemporally adaptive whole-brain functional imaging experiment is shown as a function of time in Supplementary Video 9. (c) Top, enlarged view of the image regions marked by orange boxes in b. Bottom, intensity line profile across three adjacent neurons, corresponding to the cyan lines in the image data shown above. Black arrows indicate the location of cell boundaries. Non-adaptive imaging fails to resolve individual cell identities, whereas adaptive imaging recovers and maintains single-cell resolution. (d) Adaptive whole-brain imaging was performed for a total period of 20 h using an interleaved imaging scheme that acquires one complete brain volume every 375 ms and alternates between corrected (blue) and uncorrected (red) microscope states in subsequent volumetric scans. Both versions of the experiment start with the same initial (optimized) microscope state, i.e., all microscope parameters are identical at time point 0. Single-neuron activity traces are shown for two pairs of neurons in the forebrain region highlighted by a green box in a. One set of activity traces (A,B) shows high-speed functional data for a 3-min period at the 1-h mark of the experiment, whereas the other set (C,D) shows data at the 11-h mark. The fidelity of single-neuron activity traces is substantially improved by adaptive imaging already in the early phase of the time-lapse recording (1 h). In the late phase (11 h), further degradation of image quality and data fidelity affects multiple brain regions in the uncorrected image data, for which high resolution and image contrast is restored by AutoPilot-mediated microscope adaptation (Supplementary Video 9). Scale bars, 20 μm (b), 5 μm (c), 10 μm (d).

of view (Fig. 5b,c). The AutoPilot framework thus computationally maps and corrects the 3D light-sheet path across the specimen volume using a robust image-based algorithm for continuous optimization of light-sheet angles α_i and β_i (Supplementary Fig. 11). This algorithm operates on the same defocus image sequences used to correct the offsets of light-sheet and detection focal planes (I_1 , I_2 , D_1 and D_2), which eliminates the need for additional measurements and optimizes the use of time and photon budget (Fig. 5d). Compensating for light-sheet refraction in a spatially adaptive manner is essential to improve resolution systematically across a large field of view and cannot be replaced by adaptive imaging limited to translational degrees of freedom (Fig. 5e).

In addition to quantifying resolution improvements in multiple model systems for the full set of AutoPilot parameters, we quantitatively investigated the causes and impacts of divergence between light-sheet and detection focal planes in the absence of angular degrees of freedom. We measured α_i and β_i deflection angles in a *Drosophila* embryo as function of depth (Supplementary Fig. 17) and formulated a theoretical model of light-sheet propagation considering the optical and geometrical properties of the embryo (Supplementary Methods, part 5). Optimizing spatial resolution requires continuous adjustment of β_i using nonlinear parameter trajectories spanning the intervals $[0.5^\circ\text{--}2.0^\circ]$ and $[-0.5^\circ\text{--}2.0^\circ]$ in each camera field (Fig. 5f). The need for these corrections arises from two primary optical effects (Supplementary Fig. 18). The refractive index mismatch between specimen and its environment (i) leads to location-dependent light-sheet refraction at the surface of the embryo and (ii) introduces spatially variant curvature of detection focal planes inside the specimen. These mechanisms lead to a theoretical position-dependent angular mismatch between light-sheet and detection focal planes that is in good agreement with the optimal corrections determined and executed by the AutoPilot framework in a completely data-driven manner (Fig. 5f; Supplementary Methods, part 5).

Adaptive whole-brain functional imaging in larval zebrafish

Complementing the developmental imaging applications discussed above, we also sought to apply the AutoPilot framework to spatiotemporally adaptive whole-brain functional imaging. Such experiments are frequently performed with calcium indicators that change intensity levels in response to neuronal activity²⁹ and demand substantially higher image-acquisition rates than developmental imaging experiments^{10,30}. Light-sheet refraction across the brains of 4- and 5-d-old larval zebrafish is less pronounced than that in *Drosophila* embryos (β_i is, on average, three-fold smaller; Supplementary Fig. 12d; Online Methods). However, light-sheet offsets I_i vary substantially across the brain and are furthermore dynamic in time at a spatial scale comparable to the depth of detection focus (Supplementary Fig. 12d). This suggests that whole-brain functional imaging should benefit substantially from microscope adaptation under the control of the AutoPilot framework. Taking advantage of an hs-SiMView microscope design that enables rapid piezo-based volumetric imaging from multiple views simultaneously¹⁵, we thus developed an imaging assay for high-speed functional imaging concurrently with AutoPilot-mediated system optimization.

The AutoPilot measurements and computations for both light sheets and seven reference planes spanning the 200- μm -deep brain volume take 10 s. Because of the slow drift of optical conditions in advanced developmental stages, a 10-min update frequency for the core parameter set (I_i , D_i) is sufficient for maintaining optimal image quality. The remaining 98% of microscope bandwidth can thus be reserved exclusively for high-resolution whole-brain imaging at a sustained

volume rate of 3 Hz (Supplementary Table 10). A comparison of corrected and uncorrected image data shows that adaptive functional imaging recovers single-cell resolution in multiple brain regions that cannot be resolved without microscope adaptation, and furthermore offers substantial improvements in the fidelity of single-neuron activity traces (Supplementary Video 9; Fig. 6). For example, after 1 h of imaging, image quality is still comparable in midbrain regions, but uncorrected images of forebrain regions suffer from substantial degradation (Fig. 6d). At the mid-point of the 20-h time-lapse experiment, image quality in large sections of both the fore- and mid-brain is substantially degraded without adaptive microscope state corrections (Supplementary Video 9).

DISCUSSION

We developed a light-sheet microscopy framework for spatiotemporally adaptive live imaging. This framework effectively yields a 'smart' light-sheet microscope^{30,31} capable of substantially improving spatial resolution by continuously and automatically adapting to the dynamic optical conditions encountered in living specimens. We demonstrated that this framework offers robust performance for a wide variety of model systems, fluorescent markers strategies and imaging assays. Complementing the data presented in this paper, we deployed the AutoPilot framework on three different types of light-sheet microscopes operated by a user group of, in total, ten researchers with different backgrounds. These AutoPilot-controlled light-sheet microscopes have been in use for over 2 years, allowing us to continuously improve the AutoPilot framework and turn it into a robust method. The high level of automation realized by our approach thus also simplifies the use of light-sheet microscopes by non-experts: users with limited imaging experience are able to consistently obtain optimal data quality, even when working with challenging biological specimens or executing complex imaging workflows.

The key ideas underlying the AutoPilot framework follow general design principles that can be readily applied to other types of light-sheet microscopes. Our method is not constrained to a particular mode of fluorescence excitation and is thus applicable to two-photon imaging^{16,32,33}, Bessel beams^{34,35} and lattice light sheets⁹. Conceptually, this framework generalizes to microscope designs with an arbitrary number of illumination and detection arms and can easily operate additional degrees of freedom if needed. The software is made publically available as the open-source AutoPilot project (the version used for data generation for this paper is provided as Supplementary Software, but readers are encouraged to obtain the most up-to-date version from <https://microscopeautopilot.github.io>).

Our framework for spatiotemporally adaptive imaging also lays a foundation for light-sheet based adaptive optics in large living specimens. The AutoPilot-mediated optimization of spatial overlap between light-sheet and detection focal planes is a key prerequisite to this end. Our framework could thus be further extended to operate wavefront sensors, spatial light modulators and deformable mirrors in the microscope's illumination and detection arms, which would enable complementary optical corrections.

The high resolution and system automation achieved with our adaptive imaging framework furthermore open the door to high-throughput assays for high-resolution live imaging of large biological specimens. In addition to benefitting essentially any investigation requiring high-resolution *in vivo* data of multicellular organisms, we envision that our method will enable the use of light-sheet microscopy for automated drug screens, mutant screens and the construction of anatomical and developmental atlases in various biological model systems.

METHODS

Methods, including statements of data availability and any associated accession codes and references, are available in the [online version of the paper](#).

Note: Any Supplementary Information and Source Data files are available in the [online version of the paper](#).

ACKNOWLEDGMENTS

We thank all members of the Keller laboratory for extensive testing of the AutoPilot framework; Tzumin Lee (Janelia Research Campus) for deadpanEE–Gal4 *Drosophila* stocks; Misha Ahrens for *Tg(elavl3:GCaMP6f)* zebrafish stocks; Nicola Maghelli for help with illustrations; Martin Weigert for 3D rendering software; Vanessa de Oliveira Carlos for *D. rerio* graphics; and Misha Ahrens, Chen Wang, Katie McDole, Kaspar Podgorski, Na Ji, Eric Betzig and Iain Patten for helpful discussions and thoughtful comments on the manuscript. This work was supported by the Howard Hughes Medical Institute, the Max Planck Institute for Cell Biology and Genetics and the German Federal Ministry of Research and Education (BMBF) under the funding code 031A099.

AUTHOR CONTRIBUTIONS

P.J.K. and L.A.R. conceived of the research and developed the AutoPilot framework. L.A.R. designed and wrote the AutoPilot core algorithms. M.C. implemented the microscope control software, with input from P.J.K. and L.A.R. R.K.C. implemented the light-sheet microscope with digitally adjustable degrees of freedom. W.C.L. performed adaptive imaging experiments of *Drosophila* embryogenesis and the zebrafish larval brain. W.C.L. and Y.W. performed adaptive imaging experiments of zebrafish embryogenesis. P.J.K. supervised the project. L.A.R. and P.J.K. wrote the paper, with input from all authors.

COMPETING FINANCIAL INTERESTS

The authors declare competing financial interests: details are available in the [online version of the paper](#).

Reprints and permissions information is available online at <http://www.nature.com/reprints/index.html>.

- Pantazis, P. & Supatto, W. Advances in whole-embryo imaging: a quantitative transition is underway. *Nat. Rev. Mol. Cell Biol.* **15**, 327–339 (2014).
- Keller, P.J. Imaging morphogenesis: technological advances and biological insights. *Science* **340**, 1234168 (2013).
- Höckendorf, B., Thumberger, T. & Wittbrodt, J. Quantitative analysis of embryogenesis: a perspective for light sheet microscopy. *Dev. Cell* **23**, 1111–1120 (2012).
- Winter, P.W. & Shroff, H. Faster fluorescence microscopy: advances in high speed biological imaging. *Curr. Opin. Chem. Biol.* **20**, 46–53 (2014).
- Santi, P.A. Light sheet fluorescence microscopy: a review. *J. Histochem. Cytochem.* **59**, 129–138 (2011).
- Weber, M. & Huisken, J. Light sheet microscopy for real-time developmental biology. *Curr. Opin. Genet. Dev.* **21**, 566–572 (2011).
- Stelzer, E.H. Light-sheet fluorescence microscopy for quantitative biology. *Nat. Methods* **12**, 23–26 (2015).
- Wu, Y. *et al.* Spatially isotropic four-dimensional imaging with dual-view plane illumination microscopy. *Nat. Biotechnol.* **31**, 1032–1038 (2013).
- Chen, B.C. *et al.* Lattice light-sheet microscopy: imaging molecules to embryos at high spatiotemporal resolution. *Science* **346**, 1257998 (2014).
- Chhetri, R.K. *et al.* Whole-animal functional and developmental imaging with isotropic spatial resolution. *Nat. Methods* **12**, 1171–1178 (2015).
- Wu, Y. *et al.* Inverted selective plane illumination microscopy (iSPIM) enables coupled cell identity lineaging and neurodevelopmental imaging in *Caenorhabditis elegans*. *Proc. Natl. Acad. Sci. USA* **108**, 17708–17713 (2011).
- Ahrens, M.B., Orger, M.B., Robson, D.N., Li, J.M. & Keller, P.J. Whole-brain functional imaging at cellular resolution using light-sheet microscopy. *Nat. Methods* **10**, 413–420 (2013).
- Fahrbach, F.O., Voigt, F.F., Schmid, B., Helmchen, F. & Huisken, J. Rapid 3D light-sheet microscopy with a tunable lens. *Opt. Express* **21**, 21010–21026 (2013).
- Capoula, J., Wachsmuth, M., Hufnagel, L. & Knop, M. Quantitative fluorescence imaging of protein diffusion and interaction in living cells. *Nat. Biotechnol.* **29**, 835–839 (2011).
- Lemon, W.C. *et al.* Whole-central nervous system functional imaging in larval *Drosophila*. *Nat. Commun.* **6**, 7924 (2015).
- Tomer, R., Khairy, K., Amat, F. & Keller, P.J. Quantitative high-speed imaging of entire developing embryos with simultaneous multiview light-sheet microscopy. *Nat. Methods* **9**, 755–763 (2012).
- Kaufmann, A., Mickoleit, M., Weber, M. & Huisken, J. Multilayer mounting enables long-term imaging of zebrafish development in a light sheet microscope. *Development* **139**, 3242–3247 (2012).
- Keller, P.J., Schmidt, A.D., Wittbrodt, J. & Stelzer, E.H.K. Reconstruction of zebrafish early embryonic development by scanned light sheet microscopy. *Science* **322**, 1065–1069 (2008).
- Keller, P.J. *et al.* Fast, high-contrast imaging of animal development with scanned light sheet-based structured-illumination microscopy. *Nat. Methods* **7**, 637–642 (2010).
- Huisken, J., Swoger, J., Del Bene, F., Wittbrodt, J. & Stelzer, E.H.K. Optical sectioning deep inside live embryos by selective plane illumination microscopy. *Science* **305**, 1007–1009 (2004).
- Wang, K. *et al.* Rapid adaptive optical recovery of optimal resolution over large volumes. *Nat. Methods* **11**, 625–628 (2014).
- Wang, C. *et al.* Multiplexed aberration measurement for deep tissue imaging in vivo. *Nat. Methods* **11**, 1037–1040 (2014).
- Quirin, S. *et al.* Calcium imaging of neural circuits with extended depth-of-field light-sheet microscopy. *Opt. Lett.* **41**, 855–858 (2016).
- Tomer, R. *et al.* SPED light sheet microscopy: fast mapping of biological system structure and function. *Cell* **163**, 1796–1806 (2015).
- Turaga, D. & Holy, T.E. Image-based calibration of a deformable mirror in wide-field microscopy. *Appl. Opt.* **49**, 2030–2040 (2010).
- Turaga, D. & Holy, T.E. Aberrations and their correction in light-sheet microscopy: a low-dimensional parametrization. *Biomed. Opt. Express* **4**, 1654–1661 (2013).
- Masson, A. *et al.* High-resolution in-depth imaging of optically cleared thick samples using an adaptive SPIM. *Sci. Rep.* **5**, 16898 (2015).
- Bourgenot, C., Saunter, C.D., Taylor, J.M., Girkin, J.M. & Love, G.D. 3D adaptive optics in a light sheet microscope. *Opt. Express* **20**, 13252–13261 (2012).
- Chen, T.W. *et al.* Ultrasensitive fluorescent proteins for imaging neuronal activity. *Nature* **499**, 295–300 (2013).
- Keller, P.J. & Ahrens, M.B. Visualizing whole-brain activity and development at the single-cell level using light-sheet microscopy. *Neuron* **85**, 462–483 (2015).
- Scherf, N. & Huisken, J. The smart and gentle microscope. *Nat. Biotechnol.* **33**, 815–818 (2015).
- Truong, T.V., Supatto, W., Koos, D.S., Choi, J.M. & Fraser, S.E. Deep and fast live imaging with two-photon scanned light-sheet microscopy. *Nat. Methods* **8**, 757–760 (2011).
- Palero, J., Santos, S.I., Artigas, D. & Loza-Alvarez, P. A simple scanless two-photon fluorescence microscope using selective plane illumination. *Opt. Express* **18**, 8491–8498 (2010).
- Planchon, T.A. *et al.* Rapid three-dimensional isotropic imaging of living cells using Bessel beam plane illumination. *Nat. Methods* **8**, 417–423 (2011).
- Fahrbach, F.O., Simon, P. & Rohrbach, A. Microscopy with self-reconstructing beams. *Nat. Photonics* **4**, 780–785 (2010).
- Keller, P.J. *Microtubule Dynamic Instability Analyzed in Three Dimensions Over Time with Selective Plane Illumination Microscopy and Modeling of Yeast Sporulation*. Diploma thesis, University of Heidelberg. (2005).
- Duck, F.A. *Physical Properties of Tissue: A Comprehensive Reference Book* (Academic Press Inc., San Diego, 1990).

ONLINE METHODS

Note. The following sections provide only a brief overview of the methods associated with this study. A detailed description of the framework for spatiotemporally adaptive imaging and all associated methodological concepts is provided in **Supplementary Methods**, parts 1–6, which include the design of the multi-view light-sheet microscope with digitally controlled light-sheet and detection plane geometries, architecture of the real-time software layer, design and evaluation of image quality metrics, algorithms for computational reconstruction of three-dimensional light-sheet geometry, special and general optimization theories underlying the AutoPilot framework, and computational approaches to quantifying improvements in spatial resolution.

Sample preparation and spatiotemporally adaptive live imaging of *Drosophila* embryos. All *Drosophila* embryos used in this study (**Supplementary Videos 1–4, 8 and 10; Figs. 2, 4 and 5**) carried ubiquitously expressed histone tagged with RFP (w; His2Av::mRFP1; +, Bloomington stock #23560). For two-color recordings, nuclear-labeled females who also carried the deadpanEE-Gal4 driver, which expresses in early neuroblasts and their progeny (w; His2Av::mRFP1; deadpanEE-Gal4), were crossed with males with the ubiquitous nuclear label and membrane-tethered GFP under UAS control (10XUAS-IVS-myr::GFP; Bloomington stock #32197) that was combined into a single homozygous stock (w/y; His2Av::mRFP1; 10XUAS-IVS-myr::GFP). Freshly laid embryos were collected by placing a large population of adult flies on grape-juice agar plates for 1 h. The embryos were collected and dechorionated with 50% bleach solution for 1 min followed by thorough rinsing in tap water. Dechorionated embryos were embedded in 1.2% low-melting-temperature agarose in a custom-built glass capillary (1.5 mm inner diameter, 20 mm length; Hilgenberg GmbH). The fully gelled agarose was extruded from the capillary until the embryo was completely exposed outside the glass. The capillary was held upright from below in the tap-water-filled recording chamber of the light-sheet microscope.

Detailed information on the configuration of the AutoPilot framework in *Drosophila* adaptive-imaging experiments is provided in **Supplementary Tables 5, 6 and 9**.

Sample preparation and spatiotemporally adaptive live imaging of zebrafish embryos. Zebrafish embryos from the transgenic line Tg(β -actin:H2B-eGFP) homozygous for ubiquitous nuclear-localized GFP (**Supplementary Videos 5–7; Fig. 3**) were embedded in 0.5% low-melting-point agarose (Type VII, Sigma-Aldrich) encased within a Teflon FEP tube with 25- μ m-thick walls (Zeus). This tube was held in place by a custom-built glass capillary (2.5 mm inner diameter, 20 mm length; Hilgenberg GmbH). The capillary itself was mounted vertically in the sample chamber filled with filtered fish facility water. The embryo was oriented in the soft agarose gel such that the animal and vegetal poles were each facing one of the microscope's detection objectives. Specimens were maintained at room temperature throughout the imaging period. After each experiment, specimens were kept in a Petri dish for several days to control for normal development.

To establish controls for sample physiology and normal development, additional control embryos were placed in the microscope sample chamber together with the respective embryo used for imaging (referred to below as the “experiment specimen”). In contrast to the embryo used for imaging, control embryos were not directly exposed to laser light during the experiment. At 3 d post-fertilization (dpf), control and experiment specimens were imaged on an Olympus MVX10 microscope to confirm normal physiology and development of the experiment specimen (**Supplementary Fig. 19**).

Detailed information on the configuration of the AutoPilot framework in zebrafish adaptive imaging experiments is provided in **Supplementary Tables 7 and 8**.

Sample preparation and spatiotemporally adaptive whole-brain functional imaging in zebrafish. Zebrafish from the transgenic line Tg(*elavl3:GCaMP6f*) expressing the calcium indicator GCaMP6f pan-neuronally were crossed with *casper* or *nacre* transgenic lines, and embryos were raised at 28.5 °C until 4 dpf for long-term functional imaging and until 5 dpf for short-term functional imaging. Larval zebrafish were then paralyzed by brief immersion in 1 mg/ml α -bungarotoxin solution (Invitrogen). Once paralyzed the fish were

embedded in the center of a custom-designed glass capillary (2 mm outer diameter, 20 mm length; Hilgenberg GmbH) filled with low-melting-point agarose (SeaPlaque, Lonza) prepared in filtered fish facility water. Agarose concentrations of 1.0% and 1.2% were used for long- and short-term imaging, respectively (**Supplementary Video 9; Fig. 6; Supplementary Fig. 12**). The fully gelled agarose was extruded from the capillary until the larval zebrafish was completely exposed outside the glass. For imaging, the capillary was mounted in the microscope sample chamber filled with filtered fish facility water such that the dorsal side of the head of the larval zebrafish was facing the camera. For short-term imaging (**Supplementary Fig. 12a–c**), specimens were maintained at room temperature. For long-term functional imaging (**Supplementary Video 9; Supplementary Fig. 12d**), specimens were maintained at 26.5 °C throughout the imaging period, using specimen chamber perfusion at a rate of 6.6 ml/min (corresponding to the turnover of one full chamber volume every 4 min).

Detailed information on the configuration of the AutoPilot framework in zebrafish functional imaging experiments presented in this study is provided in **Supplementary Table 10**.

Multi-view light-sheet microscope for spatiotemporally adaptive imaging.

The light-sheet microscope for spatiotemporally adaptive imaging is conceptually based on a SiMView instrument layout¹⁶ with four orthogonal optical arms, including two arms for laser light-sheet illumination and two arms for camera-based fluorescence detection. The modified microscope design for spatiotemporally adaptive imaging uses illumination and detection arms capable of precise translation of light sheets and detection focal planes as well as precise three-dimensional rotation of light sheets. The respective ten geometrical degrees of freedom are digitally controlled to enable full automation of the microscope for spatiotemporally adaptive imaging. A detailed description of the microscope, including an overview of all mechanical, optical, electronic and computational components, is provided in **Supplementary Methods**, part 1, and **Supplementary Table 11**. A computer model of the light-sheet microscope, which uses a color code to identify microscope components associated with the ten primary degrees of freedom, is shown in **Supplementary Figure 1**. An illustration of the concepts underlying control of light-sheet roll and yaw angles is provided in **Supplementary Figure 2**. Multi-view image processing and lossless compression of acquired image data using the KLB file format were performed as previously described³⁸.

Real-time microscope control framework. The microscope control framework uses a distributed architecture, with the user interface, image acquisition and data management software located on a high performance workstation and the instrument control, waveform generation, and experiment sequencing control software located on a real-time control system. The host computer and the real-time controller communicate via a TCP/IP server client architecture. The custom microscope control software consists of three primary modules, including the AutoPilot libraries and two modules for microscope control:

- (1) A software layer for real-time instrument control, waveform generation, experiment sequencing and synchronization of all electronics components used in the microscope. This module was developed in the 32-bit LabVIEW environment and is deployed on a PXI-8110 real-time control system (National Instruments). The PXI chassis also holds four PXI-6733 8-channel analog output modules, which are used to control galvanometer scanners, laser systems, camera triggers, piezo positioners, Pockels cell and shutter states. Other PXI modules are used to control filter wheels and sample stage motion.
- (2) A front end that consists of software modules for receiving, processing and online visualization of image data streams, and a graphical user interface (GUI) for configuring imaging experiments and AutoPilot-based microscope control. This module was developed in the 64-bit LabVIEW environment (National Instruments) and is deployed on the high-performance host computer.
- (3) A set of AutoPilot libraries facilitating all core computations and system optimization associated with the AutoPilot framework. These libraries were written in Java and C/C++.

There are two distinct modes of AutoPilot operation: the Initial System Optimization before an experiment and Microscope State Updates during an experiment. Typically, users of the AutoPilot framework conduct an Initial System Optimization routine, which automatically determines the values to use for each degree of freedom for each reference location in the specimen and for each wavelength, by executing multiple converging iterations of microscope state adaptation. Then, during an experiment, Microscope State Updates (assumed to be small corrections) occur at user-defined intervals between experimental time points, ensuring continuous spatiotemporal adaptation of the microscope to dynamic changes in morphology and optical properties of the specimen, fluorescent marker distributions inside the specimen and optical properties of the specimen environment. The design and function of the AutoPilot framework is described in detail in **Supplementary Methods**, part 1–5, and key components are also summarized in the methods sections below.

Design and performance benchmark of image quality metrics. We implemented 30 conventional and modified image quality metrics and screened these candidate metrics to identify the optimal metric for our framework for spatiotemporally adaptive imaging. To this end, we systematically evaluated the performance of each image quality metric using synthetic- as well as real-data benchmarks, using 66 manually annotated light-sheet microscopy focus stacks of different types of biological specimens and fluorescent marker strategies (**Supplementary Methods**, part 2). The normalized DCT Shannon entropy (DCTS) achieved the best overall performance, providing the best focus localization accuracy, a high signal-to-background ratio, an exceptionally low density of local maxima, and a fast median image data throughput of 1 pixel per 27 ns (**Supplementary Tables 1–4**). The DCTS metric is defined as follows:

$$\text{DCTS}_{r_o}(I) \stackrel{\text{def}}{=} -\frac{2}{r_o^2} \sum_{x+y < r_o} \left| \frac{\mathcal{F}_c(I)_{x,y}}{L_2(\mathcal{F}_c(I))} \right| \text{abslog}_2 \left(\frac{\mathcal{F}_c(I)_{x,y}}{L_2(\mathcal{F}_c(I))} \right) \quad (1)$$

$$\text{with } \text{abslog}_b(x) = \begin{cases} \log_b x & \text{if } x > 0 \\ \log_b -x & \text{if } x < 0 \\ 0 & \text{if } x = 0 \end{cases}$$

In equation (1), r_o is the support radius of the optical transfer function (OTF) of the microscope, $\mathcal{F}_c(I)$ is the discrete cosine transform (DCT II) and $L_2(I)$ is the 2-norm of image I (see **Supplementary Methods**, part 2, for details). For images acquired with a light-sheet waist of 3 μm (full-width at half-maximum, FWHM) and a detection NA of 0.8, the DCTS scored median and mean focus localization errors of 0 and 330 nm, respectively, thus emerging as a near-perfect focus measure in our benchmarks. The mean focus localization error of the DCTS is five-fold smaller than the depth of focus of the microscope's detection systems (1.75 μm), which are equipped with Nikon 16 \times /0.8 water-dipping objectives and Hamamatsu Orca Flash 4.0 sCMOS cameras with a pixel pitch of 6.5 μm . DCTS performance was furthermore vastly superior to that of other typical focus measures using for example, normalized variance or ratio of high/low frequencies in the Fourier spectrum, which scored median errors >1 μm and mean errors >3 μm (see **Supplementary Table 3** for details).

Special and general optimization theories for spatiotemporally adaptive light-sheet imaging. We developed a mathematical theory and the respective algorithms for system optimization in spatiotemporally adaptive imaging, considering light-sheet microscopes with an arbitrary number of spatiotemporally adjustable degrees of freedom (**Supplementary Methods**, parts 3 and 4). The special theory treats different color channels and different spatial locations in the specimen independently, whereas the general theory considers measurements associated with all spatial locations and color channels simultaneously to determine a globally optimal system state.

This general framework is suitable for optimizing the system state of microscopes with any number of illumination and detection arms and for any number of color channels, considering arbitrary subsets of parameters for adjusting lateral or axial light-sheet offsets, light-sheet roll and yaw angles and detection focal plane offsets. Several modes of microscope operation are

available, offering for example, the possibility of instantaneous local system corrections (**Supplementary Methods**, part 3) or global system optimization based on spatiotemporally distributed measurements (**Supplementary Methods**, part 4). The theory and related algorithms furthermore robustly handle on-demand spatiotemporally adaptive imaging of signals that are variable in space and time. A detailed description of the methodology is provided in the **Supplementary Methods**, parts 3 and 4.

Image-based mapping of 3D light-sheet geometry in live specimens.

Restoration of co-planarity of light-sheet and detection focal planes critically requires measurement and correction of the positions of detection focal planes (D), lateral light-sheet offsets (l), axial positions of light-sheet waists (Y), and the relative angles between these planes (α and β). In order to perform these measurements robustly inside live specimens using a variety of fluorescent marker strategies, we developed an algorithm capable of computing angular degrees of freedom α and β of the 3D light-sheet optical path from the same defocus stacks used to optimize D and l . By operating on the same input data, this approach thus minimizes time spent on data acquisition and optimizes the use of the specimen's photon budget. The fully automated method and all related algorithmic concepts are described in detail in **Supplementary Methods**, part 5. Briefly, we first identify the geometrical outline of the specimen in the image stack, determine the direction of light-sheet propagation, subdivide the image stack into a grid of sub-regions (or tiles) and compute the DCTS metric for each grid point (**Fig. 5d**). This yields the optimal focus position d at each grid coordinate (x, y) . These data points collectively form a 3D point cloud in (x, y, d) space. After discarding outliers and unreliable data points identified through statistical tests, we apply a robust plane fitting algorithm to the remaining data points. From the parameters characterizing this plane we can then directly deduce the two angles α and β .

Theoretical modelling of optimal light-sheet correction angles. To investigate the spatial relationship between 3D light-sheet optical paths and 3D geometries of detection focal planes inside live specimens, we formulated a ray optics theoretical model that explicitly considers differences in refractive indices in specimen and the surrounding support matrix/medium (focusing on ovoid-like specimen geometries, such as those encountered in *Drosophila* embryos). This model is described in detail in **Supplementary Methods**, part 5 (section “Ray optics model for interpreting experimentally observed β -deflections”). The good qualitative and quantitative agreement between theoretical predictions and experimental measurements of the optimal, depth-dependent light-sheet angle β (**Fig. 5f**; **Supplementary Figs. 17 and 18**) suggests two primary sources of depth-dependent angular mismatches between light-sheet and detection focal planes *in vivo*: (i) refraction of light sheets at the matrix-to-embryo interface, and (ii) curvature of the detection focal plane as a result of a lensing effect introduced by the embryo in the detection path.

Spatial resolution analysis. In order to assess improvements in spatial resolution by adaptive imaging *in vivo*, we developed a computational strategy for estimating relative differences in spatial resolution from image data of specimens lacking point-like sources of fluorescence. This capability is essential for evaluating microscope performance in long-term live-imaging experiments, in which injection of fluorescent beads into the living specimen is not a realistic option as it would endanger sample physiology when performed systematically across the volume of the specimen. Our computational solution takes advantage of sharp edges at the boundaries of fluorescent objects (such as cell nuclei) to estimate relative differences in resolution from pairs of images acquired under different optical conditions but for the same specimen region. The quantifications provided by this approach represent lower-bound estimates of the improvement in spatial resolution obtained in adaptively corrected vs. uncorrected microscope states. Please see **Supplementary Methods**, part 6, for a detailed description and mathematical derivation of this method. Complementing this resolution analysis, we furthermore evaluated the Fourier spectra of images acquired in corrected and uncorrected microscope states in order to quantify relative changes in cut-off radii in frequency space.

AutoPilot open-source project. In order to support the dissemination of the advances presented in this work, we make all software libraries developed for

our framework for spatiotemporally adaptive imaging publicly available as the open-source AutoPilot project (<https://microscopeautopilot.github.io>). This public resource includes our core algorithms for computing image quality metrics, image-based mapping of 3D light-sheet geometry inside living specimens, and special and general system optimization in a wide range of light-sheet microscopes. The source code includes a full software documentation. Detailed information on the mathematical basis and principles underlying the framework for spatiotemporally adaptive imaging are provided in the **Supplementary Materials**.

The open-source project provides all core algorithms in the Java programming language, C bindings for easy interfacing with LabVIEW and MATLAB bindings for offline testing and data analysis. Since our reference implementation

is written in Java, the framework can easily be integrated in existing Java-based microscope control software packages, such as Micro-Manager³⁹ and the open source light-sheet microscopy platform openSPIM⁴⁰.

38. Amat, F. *et al.* Efficient processing and analysis of large-scale light-sheet microscopy data. *Nat. Protoc.* **10**, 1679–1696 (2015).
39. Edelstein, A., Amodaj, N., Hoover, K., Vale, R. & Stuurman, N. Computer control of microscopes using μ Manager. *Curr. Protoc. Mol. Biol.* **92**, 14.20.1–14.20.17 (2010).
40. Pitrone, P.G. *et al.* OpenSPIM: an open-access light-sheet microscopy platform. *Nat. Methods* **10**, 598–599 (2013).